Pair Interaction Lattice Gas Simulations: Flow Past Obstacles in Two and Three Dimensions

Armin Vogeler[1] and Dieter A. Wolf-Gladrow[1]

Apart from the FCHC (face-centered hypercube), Nasilowski's pair interaction lattice gas (PI) is the only known lattice gas automaton for three-dimensional hydrodynamic simulations. Unfortunately, the viscosity of PI is not isotropic. In order to determine the degree anisotropy, we derive fluid dynamic equations for the regime of compressible viscid flow. From relaxation measurements of waves propagating in various directions we compute the physically relevant dissipation coefficients and compare our results with theoretical predictions. Although PI shows a high degree of anisotropy, we define the mean value of the dissipation tensor as effective shear viscosity. Using this value of $v_{\text{eff}}^{2D} = 0.35$, two-dimensional simulations of flow past a cylinder yield drag coefficients in quantitative agreement with wind tunnel measurements over a range of Reynolds numbers of 5–50. Three-dimensional simulations of flow past a sphere yield qualitative agreement with various references. A fit of the results to a semi-empirical curve provides an effective value of $v_{\text{eff}}^{3D} = 0.21$ for a range of Reynolds numbers from 0.19 to 40. In order to check for finite-size effects, we measured the mean free path λ and computed the Knudsen numbers. We obtained $\lambda \approx 1$ lattice unit, corresponding to $\text{Kn} = 0.01$ (2D) and $\text{Kn} = 0.1$ (3D). We found no significant finite-size effects.

KEY WORDS: Viscosity measurements; drag coefficients; 3D simulations; finite-size effects.

1. INTRODUCTION

In 1986 Frisch, Hasslacher, and Pomeau (FHP)[13] (also see Frisch *et al.*[12] and Wolfram[43]) proved that a certain cellular automaton lattice gas shows fluid-like behavior in the macroscopic limit or more precisely that mean quantities obey the two-dimensional Navier–Stokes equations.

---

[1] Alfred-Wegener-Institute for Polar and Marine Research, D-2850 Bremerhaven, Germany.

This work showed for the first time that lattice gases are an alternative to common numerical techniques in modeling fluid dynamics. The idea of lattice gases is rooted in the knowledge that the form of the dynamical equations of a fluid is entirely determined by inherent microscopic symmetries and conservation laws. While finite-difference and finite-element methods solve discretized Navier–Stokes equations with all the well-known problems of these methods, the lattice gas method discretizes the phase space of a simplified ideal gas. This results in simple and numerical well-behaved algorithms well suited for parallel computation.

The paper by Frisch *et al.* initiated rapidly increasing interest in cellular automata as a tool for solving complex physical problems. Good examples are flow through porous media,[34] acoustic wave propagation in inhomogeneous media,[19] a model for surface tension,[1] and the simulation of various simple boundary layer problems.[26]

In the last few years many lattice gas automata (LGA) have been proposed for hydrodynamic simulations.[4,28] The original FHP model has been extended by the introduction of rest particles and appropriate collision rules[8]; colored particles have been added to simulate two-phase flow such as immiscible fluids,[35] stratified fluids,[23] and autocatalytic reactions.[5] Even external forces can be incorporated for plasma flow simulations.[29]

Although a lattice gas was already proposed for three-dimensional hydrodynamic simulations in 1986 by d'Humières *et al.*,[9] only very few applications have been reported. One of the reasons may be the extremely complicated collision rules of this "face-centered hypercube" (FCHC) model.[17] An interesting alternative to the FCHC model is the pair interaction lattice gas (PI) proposed by Nasilowski.[30] This lattice gas runs in arbitrary dimensions and has simple collision rules. But there is no rose without a thorn: the viscosity is not isotropic. This was derived theoretically by Nasilowski. In parallel we have measured the relaxation of waves propagating in various directions and have calculated the physically relevant components of the viscosity tensor (see Section 3) which we will compare with theoretical predictions.

The degree of anisotropy is rather strong: the shear viscosity varies by a factor of two between certain angles. Therefore, one may ask if such an automaton can successfully be used in the simulation of fluid flows. To get a hint to the answer, we have chosen some well-known problems for reference: the flow past a cylinder (ideally of infinite length) and past a sphere. This is discussed in Sections 5 and 6.

2. THE PAIR INTERACTION LATTICE GAS

The dynamical behavior of a lattice gas is mainly dominated by the symmetry properties of the underlying lattice and the built-in conservation

laws. Due to insufficient symmetry of its square lattice, the first deter-
ministic lattice gas (HPP)[15] reproduces only isotropic sound waves,
whereas the momentum flux is anisotropic. Ten years later the FHP lattice
gas with the higher symmetric hexagonal lattice had success in simulating
Navier–Stokes equations. Unfortunately the FHP lattice cannot be
extended to three dimensions, so one has to proceed to four dimensions
and project the results back. But this extension of FHP, called FCHC, has
extremely complicated collision rules[17] and requires much computational
resources.

   The pair interaction lattice gas (PI) is an attempt to unify the
advantages of the HPP and the FHP/FCHC models. It was constructed
with the aim of three-dimensional hydrodynamic simulations with simple
and deterministic collision rules.

   In this section we describe the pair interaction lattice gas. For brevity
we restrict ourselves to a more phenomenological presentation. Readers
more interested in the explicit derivation of the statistics and the fluid
dynamical equations are referred to Nasilowski.[30]

   In order to realize arbitrary dimensionality, PI adopts the square lat-
tice from the HPP lattice gas in spite of its insufficient symmetry proper-
ties, but only the nodes with even or odd coordinate pairs are used (see
Fig. 1). In D dimensions each node consists of 2^D cells, corresponding to
the 2^D links to the nearest neighbors. A cell can be occupied by at most one
particle (exclusion principle). The updating (time step) is composed of two
successive steps as usual, the interaction between cells and the propagation
of the particles to the nearest-neighbor nodes.

   Now the required symmetry to force the momentum advection term to
be isotropic is provided by an additional degree of freedom, due to a some-
what strange definition of the momentum of the particles: The momentum
$\mathbf{m}_i$ of a cell i is defined componentwise by

$$m_{i\alpha} := n_i h_{i\alpha} c_{i\alpha}, \qquad i = 1,..., 2^D; \quad \alpha = 1,..., D \tag{1}$$
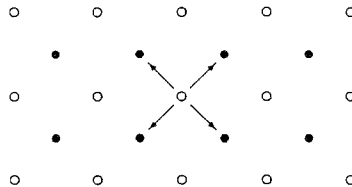

Fig. 1.   Lattice structure of the PI model in two dimensions. Particle positions at even and
odd times are shown as white and black circles, respectively. The arrows indicate the four
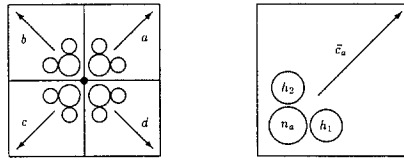possible particle velocities.

Fig. 2. The cellular structure of the PI model. Left: All the local cells (indicated by the squares) belonging to one of the lattice nodes (indicated by the dot in the middle). Right: One of the cells in more detail. Each circle corresponds to a bit in the computer.

where $n_i \in \{0, 1\}$ is the mass bit, $h_{i\alpha} \in \{0, 1\}$ is the momentum component and $c_{i\alpha} = \pm 1$ is the component of the propagation velocity. Thus the momentum is represented by D additional independent bits, corresponding to D components. This allows the momentum to be not necessarily parallel to the propagation velocity of the cell; instead it fluctuates around this direction as shown in Fig. 2.

The collision step consists of successive interactions between pairs of cells along the coordinate axes (Fig. 3 shows this for the two-dimensional case). Possible collisions are constructed according to the conservation laws for mass and momentum and according to the strategy to exchange as much as possible in order to minimize dissipation.[18] A symbolic description of the collision rules is given in Fig. 4 as an example for a horizontal pair. Due to the modular structure of this lattice gas, the interaction rules are the same for any pair of cells in any dimension. This simplifies the code and the extension to higher dimensions.

2.1. Hydrodynamic Equations

As expected for a lattice gas with exclusion principle, Nasilowski gets a distribution function of Fermi–Dirac-type for the occupation of a cell. In a similar way as this has been done for FHP/FCHC models, he obtains the
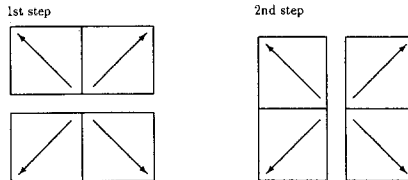

Fig. 3. Subsequent formation of horizontal and vertical pairs of interacting cells in the collision process. The "process" is instantaneous (it takes no time in the model) and local (it does not involve any cells located at different lattice points). The squares represent the four local cells; their velocity vectors are indicated by the arrows.
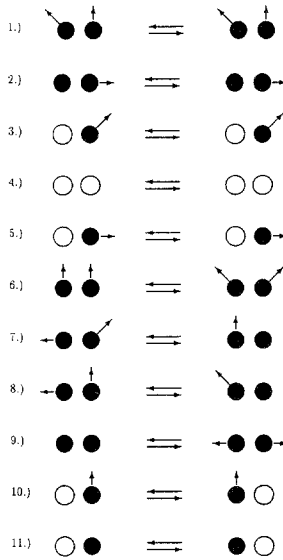
Fig. 4. The pair interaction rules, illustrated for a "horizontal" interaction between cells a and b. Black circles indicate occupied cells and white circles indicate empty cells; the particle momentum is represented by arrows. When only one cell contains a particle and the other is empty, that particle can "spontaneously" change its velocity (jump to the partner cell) without changing its momentum (rule 10).

hydrodynamic equations for three regimes from a Chapman–Enskog-type expansion:

(a) Inviscid, incompressible flow

(b) Inviscid, compressible flow

(c) Viscid, incompressible flow

The lattice gas shows weak compressible behavior. To analyze the dissipation of the compressible effects, we have to derive the hydrodynamic equations for the fourth regime, namely viscid, compressible flow. The hydrodynamic variables, the mass density per cell ρ and the momentum flux density $\mathbf{q}$, are defined by

$$\rho := 2^{-D} \sum_i \langle n_i(\mathbf{r}_*, t_*) \rangle \tag{2}$$

$$\mathbf{q} := 2^{-D} \sum_i \langle \mathbf{m}_i(\mathbf{r}_*, t_*) \rangle \tag{3}$$

where the $\langle \cdot \rangle$ denote ensemble averaging. The subsequent derivation proceeds from Eqs. (91) and (78) in Nasilowski.[30] The mass flux M_k and

momentum flux Q_{jk} as functions of ρ and $\mathbf{q}$ including the dissipative terms with coefficients T_{jlkm} read

$$M_k = 2\,\frac{1-\rho}{2-\rho}\,q_k - \frac{1}{9}\,\partial_k \rho \tag{4}$$

$$Q_{jk} = \left[\frac{\rho}{2} - 2\,\frac{(1-\rho)(1-2\rho)}{(2-\rho)^2\,\rho}\,q_j^2\right]\delta_{jk}$$

$$+\,4\,\frac{(1-\rho)^2}{(2-\rho)^2\,\rho}\,q_j q_k - T_{jlkm}\partial_m q_l \tag{5}$$

Summation over repeated indices is implicit unless otherwise specified. Here it does not apply to the δ_{jk}. Unfortunately, the viscosity tensor T_{jlkm} is not isotropic, due to a lack of symmetry of the underlying square lattice. The macrodynamic equations arise from inserting the above fluxes in the continuity equations resulting from the built-in conservation laws

$$\partial_t \rho + \partial_k M_k = 0 \tag{6}$$

$$\partial_t q_j + \partial_k Q_{jk} = 0 \tag{7}$$

The coefficient of the undesired q_j^2 term in the momentum flux vanishes only for a mean mass density of $\rho = 0.5$. Nevertheless, small density fluctuations are needed, so we set $\rho = 1/2 + \hat{\rho}$ and obtain by Taylor expansions of the fluxes (4) and (5) with (6) and (7)

$$\partial_t \hat{\rho} + \partial_k \left(\frac{2}{3} - \frac{8}{9}\,\hat{\rho}\right) q_k - \frac{1}{9}\,\partial_k \partial_k \hat{\rho} = 0 \tag{8}$$

$$\partial_t q_j + \partial_k \left[\frac{\hat{\rho}}{2}\,\delta_{jk} + \left(\frac{8}{9} + \frac{4}{27}\,\hat{\rho}\right) q_j q_k\right] - T_{jlkm}\partial_k \partial_m q_l = 0 \tag{9}$$

It is not possible to obtain a compressible hydrodynamic regime including dissipation without terms of mixing orders in the expansion parameter ε of the Chapman–Enskog-type expansion. This is similar to the FHP lattice gas (compare Frisch et al.[12]).

We distinguish two cases:

1. Very small deviations of the density

2. Density fluctuations comparable to the momentum flux

For the first case of very small density fluctuations compared to the momentum flux we assume the following orders of magnitude:

$$\hat{\rho} = O(\varepsilon^2), \qquad \mathbf{q} = O(\varepsilon), \qquad \partial_t = O(\varepsilon), \qquad \partial_r = O(\varepsilon) \tag{10}$$

Up to $O(\varepsilon^3)$ we get the hydrodynamic equations for slightly compressible flow with $\frac{8}{9}\mathbf{q} = \mathbf{u}$ and $\frac{4}{3}\hat{\rho} = \rho'$,

$$\partial_t \rho' + \partial_k u_k = 0 \tag{11}$$

$$\partial_t u_j + \partial_k (u_j u_k + p\delta_{jk}) - T_{jlkm}\partial_k \partial_m u_l = 0 \tag{12}$$

For the pressure p we used the "isothermal" relation $p = c_s^2 \rho'$, with $c_s = \sqrt{\frac{1}{3}}$ being the speed of sound. The value of c_s was confirmed by our previous measurements.[42] When the density perturbation is of the same order of magnitude as the momentum flux we have

$$\hat{\rho} = O(\varepsilon), \qquad \mathbf{q} = O(\varepsilon), \qquad \partial_t = O(\varepsilon), \qquad \partial_r = O(\varepsilon) \tag{13}$$

This alters only the continuity equation. Using the above relations for ρ' and $\mathbf{u}$, the equations for the full compressible regime up to $O(\varepsilon^3)$ read

$$\partial_t \rho' + \partial_k u_k - \partial_k \rho' u_k - \tfrac{1}{9}\partial_k \partial_k \rho' = 0 \tag{14}$$

$$\partial_t u_j + \partial_k (u_j u_k + p\delta_{jk}) - T_{jlkm}\partial_k \partial_m u_l = 0 \tag{15}$$

In contrast to the slightly compressible regime (12), we obtain two additional terms in the continuity equation. The last one is an extra dissipation term, which should affect the compressional viscosity, as will be discussed below.

3. THE VISCOSITY TENSOR ACCORDING TO THEORY AND MEASUREMENTS

The first measurements of transport coefficients of the pair interaction lattice gas were by Wolf-Gladrow et al.[42] They applied two different methods in order to determine the shear viscosity and the speed of sound: Smoothing of a discontinuity in the velocity distribution and relaxation of wave-shaped velocity perturbations (see also ref. 7).

The relaxation method determines the dissipation by a measure of the relaxation of an initial wave-shaped perturbation of the velocity. The initial wave consists of a transverse and a longitudinal mode, in order to determine the shear viscosity and the bulk viscosity, respectively. The longitudinal mode induces an extra density wave. Here the components of the viscosity tensor T_{jlkm} are obtained with the relaxation method in various directions.

We restrict our considerations concerning the viscosity tensor to two dimensions because of the modular structure of the lattice gas algorithm (see previous section). Three-dimensional experiments are not expected to give any new information about the components of T_{jlkm}.

It is obvious that T_{jlkm} has to be invariant under invariance transformations of the lattice gas. In such a way the number of independent components (16 in two dimensions) can be reduced. Each transformation may be described with a matrix A_{ij} and the tensor transforms according to

$$T'_{abcd} = T_{jlkm} A_{ja} A_{lb} A_{kc} A_{md} \tag{16}$$

If A_{ij} is an element of the isometric group, then

$$T'_{abcd} = T_{jlkm} \tag{17}$$

We apply a reflection at the x_1 axis:

$$A = \begin{pmatrix} -1 & 0 \\ 0 & 1 \end{pmatrix}$$

It follows that all components with three equal indices are zero:

$$T_{1112} = T_{1222} = T_{1211} = T_{1121}$$
$$= T_{2221} = T_{2111} = T_{2122} = T_{2212} = 0 \tag{18}$$

This reduces the number of unknown components to eight.

For the subsequent derivations we will use the full compressible equations, (14), (15) since we do not know the relative magnitudes of the longitudinal density and velocity waves. But we comment on the differences from the use of the less compressible regime (11), (12) at the end of this section. If we assume **u** and the density perturbation ρ' to be small enough to drop the nonlinear terms in (14), (15), we get

$$\partial_t \rho' + \partial_j u_j - \tfrac{1}{9} \partial_k \partial_k \rho' = 0 \tag{19}$$

$$\partial_t u_j + \partial_j p - T_{jlkm} \partial_k \partial_m u_l = 0 \tag{20}$$

Based on this set of linear equations, we will determine the dissipation by measuring the relaxation of a wave-shaped velocity perturbation. The wave consists of a transverse mode with amplitude $\hat{u}_j^{\perp}$ and a longitudinal mode with amplitude $\hat{u}_j^{\parallel}$:

$$u_j(r_i, t) = [\hat{u}_j^{\perp} \exp(-\sigma t) + \hat{u}_j^{\parallel} \exp(-\theta t)] \exp(ik_l r_l) \tag{21}$$

where

$$\hat{u}_j^{\perp} k_j = 0 \tag{22}$$

$$\varepsilon_{ijk} \hat{u}_j^{\perp} k_k = 0 \tag{23}$$

ε_{ijk} is the Levi-Civita tensor. Coupled to these modes are corresponding density waves of the form

$$\rho'(r_i, t) = [\rho'^\perp \exp(-\sigma t) + \rho'^{\parallel} \exp(-\theta t)] \exp(ik_l r_l) \tag{24}$$

To determine the angular dependence, we have to apply the method in various directions relative to the lattice. First we consider the more special case of a wave of the form (21) traveling along one of the axes of the coordinate system (e.g., the x_1 axis) so that the modes of (21) separate. Then, by representing the tensor T_{jlkm} in another coordinate system rotated by an angle ϕ, we return to generality and obtain the dependence of the appropriate relaxation parameter on the angle ϕ. Therefore we use the well-known rotation matrix

$$A(\phi) = \begin{pmatrix} \cos(\phi) & \sin(\phi) \\ -\sin(\phi) & \cos(\phi) \end{pmatrix} \tag{25}$$

and obtain the rotated tensor according to (16).

1. *Transverse mode.* Inserting only the transverse mode $u_1^\perp$ in the x_1 direction in (19) and (20), it follows with (18) that

$$\rho'^\perp = 0 \tag{26}$$

$$\sigma = k_2^2 T_{1122} \tag{27}$$

as expected for a transverse wave. We obtain the relaxation parameter $\sigma(\phi)$ according to the above-described procedure using (16) with (25) and $k = k_2$:

$$\sigma(\phi) = k^2 [\alpha \cos^4(\phi) + \beta \sin^4(\phi) + \mu \sin^2(\phi) \cos^2(\phi)] \tag{28}$$

where

$$\begin{aligned} \alpha &= T'_{1122} \\ \beta &= T'_{2211} \\ \mu &= T'_{1111} + T'_{2222} - T'_{1212} - T'_{2121} - T'_{1221} - T'_{2112} \end{aligned} \tag{29}$$

2. *Longitudinal mode.* For a longitudinal mode along the x_1 axis $(k = k_1)$, Eq. (19) becomes

$$-\theta \rho'^{\parallel} + iku^{\parallel} + \tfrac{1}{9}k^2 \rho'^{\parallel} = 0 \tag{30}$$

With (18) and $p = c_s^2 \rho'$ the momentum equation (20) yields

$$-\theta u^{\parallel} + ic_s^2 k \rho'^{\parallel} + T_{1111} k^2 u^{\parallel} = 0 \tag{31}$$

Inserting (30) in (31) gives the characteristic equation

$$\theta^2 - \theta k^2 (T_{1111} + \tfrac{1}{9}) + c_s^2 k^2 + \tfrac{1}{9} k^4 T_{1111} = 0 \tag{32}$$

with solution

$$\theta_{1,2} = \frac{k^2}{2} \left(T_{1111} + \frac{1}{9} \right) \pm c_s k \left[\underbrace{\frac{k^2}{4c_s^2} \left(T_{1111} - \frac{1}{9} \right)^2}_{\leqslant 1} - 1 \right]^{1/2} \tag{33}$$

and approximately for long waves $(k \ll 1)$

$$\theta_{1,2} \approx \frac{k^2}{2} \left(T_{1111} + \frac{1}{9} \right) \pm i c_s k \tag{34}$$

with $c_s = \sqrt{\tfrac{1}{3}}$ accoding to Nasilowski.[30] The shortest wavelength used in the experiments was 95 nodes, corresponding to a wave vector of $k_{max} = 3.3 \times 10^{-2}$. Thus, the long-wave approximation is fulfilled. The imaginary part of θ $(c_s k = \omega)$ causes the relaxation of the longitudinal modes to be modulated by an oscillation in time.

In a similar way as for the transverse mode, (34) leads to the relaxation parameter $\theta(\phi)$:

$$\theta(\phi)_{1,2} \approx \frac{k^2}{2} \left[\zeta \cos^4(\phi) + \kappa \sin^4(\phi) + \tau \sin^2(\phi) \cos^2(\phi) + \frac{1}{9} \right] \pm i\omega \tag{35}$$

with

$$\zeta = T'_{1111}$$

$$\kappa = T'_{2222}$$

$$\tau = T'_{2211} + T'_{1122} + T'_{1212} + T'_{2121} + T'_{1221} + T'_{2112}$$

When the same derivation is made using the less compressible regime (11), (12) instead of Eqs. (14), (15), the term 1/9 in (35) disappears. Thus the extra dissipation term in (11) results in an offset in the relaxation of the longitudinal mode. We will check our experimental results to see if the use of the full compressible equations (14), (15) is necessary.

With the assumptions above we are now able to determine the physically relevant components of the viscosity tensor T_{jlkm} (e.g., the coefficients of the dissipative terms in the momentum equation) by measuring the relaxation of the initial velocity perturbations in various directions (represented either by the wave vector $\mathbf{k}$ or by the angle ϕ). Fitting the results of these measurements to (28) and (35) should give six coefficients containing the eight independent components of T_{jlkm}.

3.1. RELAXATION MEASUREMENTS

We performed our measurements on a square domain of 512×512 nodes with periodic boundary conditions in both directions. The relaxation curves were obtained by averaging the velocities along lines perpendicular to the wave vector at each time step. Then the components of the initial waves (21), (24) were extracted by a Fourier transformation.

Since the averaging line must be approximately steplike, the angle ϕ cannot be chosen arbitrarily. The components of the wave vector $\mathbf{k}$ have to be multiples of the x and y increments of the step algorithm in order to comply with the periodic boundary condition.

A typical set of the measured relaxation curves is shown in Fig. 5. The small oscillations of the relaxation of the transverse mode (solid line) are supposedly caused by a weak coupling to the longitudinal mode. Its strength varies with ϕ and even when solely a transverse mode is initialized a longitudinal mode of small amplitude (lower by an order of magnitude) is induced.

The relaxation parameters $\sigma(\phi)$, $\theta(\phi)$ and the speed of sound c_s are calculated by least square fits of the measured relaxation curves to expressions (28) and (35).

For sufficiently small mean velocities the results are independent of wavelength and mean velocity.

The experimental results are

$$\left.\begin{array}{l} \alpha = 0.46 \\ \beta = 0.46 \\ \mu = 0.02 \end{array}\right\} \quad \text{for the transverse mode}$$
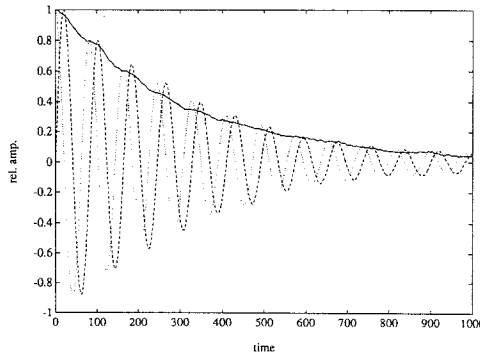

Fig. 5. A typical set of the measured relaxation curves. The exponential decay of the transverse mode and of the oscillating coupled longitudinal modes (cosine wave for $u^{\parallel}$ and sine wave for ρ') are represented as functions of time.

and

$$\left.\begin{aligned}\zeta &= 0.42\\\kappa &= 0.42\\\tau &= 1.69\end{aligned}\right\} \quad \text{for the longitudinal mode}$$

From similar calculations for other lattice gases we expect an error of the order of 10%.[12] For the speed of sound c_s we found a value of $c_s = 0.58$, a very good confirmation of the theoretical value of $c_s = \sqrt{\frac{1}{3}} \approx 0.577$. A further verification of our results is their self-consistency, since from (35) and (28) it should hold that

$$\zeta + \kappa - \mu = \tau - \alpha - \beta \tag{36}$$

$$\tag{37}$$

and we obtain values of 0.82 for the left-hand side and 0.77 for the right. Within the expected error of 10% we can consider the above relation as satisfied.

Fitting our experimental results to the relaxation of the longitudinal mode derived from the less compressible regime (11), (12) would yield

$$\left.\begin{aligned}\zeta &= 0.53\\\kappa &= 0.53\\\tau &= 1.91\end{aligned}\right\} \quad \text{for the longitudinal mode}$$

The following comparison with theoretical predictions should clarify which regime we have to use in order to achieve maximum agreement with theory.

3.2. COMPARISON WITH THEORETICAL VALUES

In parallel to our experiments Nasilowski[30] has calculated the components of the viscosity tensor in the viscid, incompressible regime using some Boltzmann-type assumptions which concern the absence of correlations between pre- and postcollision states. Although this assumption is necessary to get any result, it is not justified by any further argument.

For the longitudinal mode which is coupled to density variations, only the form of the angular distribution of the relaxation constant is reliable (Nasilowski, personal communication, 1991). From the theoretical expression of the viscosity tensor, denoted by

$$T_{jlkm} = \tfrac{1}{6}[3\delta_{jl}\delta_{km} + \delta_{jm}\delta_{kl}(1 + 2\xi_{mk}) - 2\delta_{jlkm}] \tag{38}$$

with

$$\xi_{mk} = \begin{cases} 1 & \text{for} \quad m > k \\ 0 & \text{for} \quad m \leqslant k \end{cases}$$

one gets

$$\left. \begin{array}{l} \alpha = 0.50 \\ \beta = 0.50 \\ \mu = 0 \end{array} \right\} \qquad \text{for the transverse mode}$$

and

$$\left. \begin{array}{l} \zeta = 0.33 \\ \kappa = 0.33 \\ \tau = 1.67 \end{array} \right\} \qquad \text{for the longitudinal mode}$$

Figures 6 and 7 show the experimental results and the theoretical predic-
tion according to (38) in polar representation. The relaxation of the trans-
verse mode is represented in Fig. 6 and the relaxation of the longitudinal
mode in Fig. 7.

A comparison with our measurements shows a rather good agreement
for the transverse mode: the angular distribution shows the expected form,
the values of α and β differ by only 10% from the theoretical values, and
the contribution of the μ term is negligible. At first sight one finds signifi-
cant discrepancies for the longitudinal mode if one considers ζ and κ. But
again the angular distribution of the relaxation constant shows very good
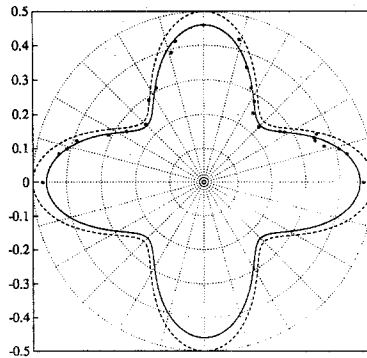agreement with the theoretical calculations.

Fig. 6. Polar representation of the relaxation of the transverse mode (shear viscosity)
$i/k^2\sigma(\phi)$ for the PI lattice gas versus angle ϕ. The fitted curve is represented by a solid line and
the measurements by asterisks. The theoretical curve is represented by the dashed line.

Fig. 7.   Polar representation of the relaxation of the longitudinal mode $2i/k^2\theta(\phi)$ for the PI lattice gas versus angle ϕ. The fitted curve is represented by a solid line and the measurements by asterisks. The theoretical curve is represented by the dashed line.

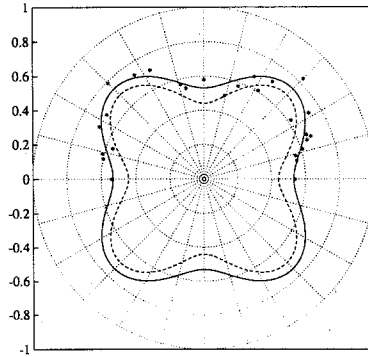Comparing our experimental results obtained by using the less compressible regime (11), (12) with the above values shows that the agreement between theory and experiment is much better when the more compressible regime is used.

Thus we determined four of the eight unknown components of the viscosity tensor. The two components in the relaxation of the transverse mode are in good agreement with theoretical values. The angular distributions of the relaxations are consistent with theoretical expectations in form and magnitude for the transverse mode and in form for the longitudinal mode.

3.3. The Effective Viscosity in Two and Three Dimensions

The relaxation measurements of the previous sections confirmed aspects of the theoretical expression of the viscosity tensor (38). Now we are interested in deriving an approximate effective shear viscosity. Its value must lie between the minimal and maximal values $v_{min} = 0.25$ and $v_{max} = 0.5$ for two dimensions. We define an effective (scalar) shear viscosity by averaging the anisotropic viscosity over the circumference of a circle.

In two dimensions the effective viscosity is therefore

$$v_{\text{eff}}^{\text{2D}} := \frac{1}{2\pi} \int_{\phi = 0}^{2\pi} v(\phi) \, d\phi \tag{39}$$

For a one-dimensional shear flow of the form $\mathbf{u} = (u_1(y, t), 0, 0)$ the momentum equation (12) becomes

$$\partial_t u_1 = T_{1122} \partial_2 \partial_2 u_1 \tag{40}$$

Via the transformation (16) we obtain the viscosity in the polar coordinates with (38)

$$\nu(\phi) = T'_{1122}(\phi) = \nu_0 [\cos^4(\phi) + \sin^4(\phi)] \tag{41}$$

This already appeared in the relaxation of the transverse mode (28). With the theoretical predicted amplitude of $\nu_0 = 0.5$ we obtain $\nu_{\text{eff}}^{\text{2D}} = 0.38$, whereas the values of the experiments of the previous section yield $\nu_0 = 0.46$ and therefore $\nu_{\text{2D}}^{\text{eff}} = 0.35$.

These approximations need experimental confirmation. Therefore we computed the drag coefficients c_D of a cylinder versus the Reynolds number R. If the qualitative relationship between c_D and R is satisfactory, the use of the effective shear viscosities should yield the best quantitative agreement with corresponding reference values.

In three dimensions the shear viscosity is expected to be anisotropic too. The computation of drag coefficients of a sphere with the three dimensional version of PI should yield an effective value for the three dimensional shear viscosity by fitting the results to corresponding reference data.

4. DRAG COEFFICIENTS FOR FLOWS PAST A CYLINDER AND A SPHERE

4.1. Stokes' Solution

The problem of viscous flow at low Reynolds numbers past a sphere or a cylinder was treated already by Stokes in 1851.[38] The Navier–Stokes equation for an incompressible fluid reads

$$\partial_t u_j + u_k \partial_k u_j = -\frac{1}{\rho} \partial_j p + \nu \partial_k \partial_k u_j \tag{42}$$

with the equation of continuity

$$\partial_j u_j = 0 \tag{43}$$

Replacing the spatial derivatives by the inverse of a characteristic length

scale L and the velocity by a speed U, one gets the following estimate for the ratio between the advection term and the friction term:

$$|u_k \partial_k u_j|/|v \, \partial_k \partial_k u_j| \approx (U^2/L)/(vU/L^2) = UL/v = R$$

where R is the Reynolds number. From this argument it seems possible to neglect the advection term for low ($\ll 1$) Reynolds numbers. For stationary flow the equation of motion then reduces to

$$0 = -\frac{1}{\rho} \partial_j p + v \, \partial_k \partial_k u_j$$

$$0 = \partial_j u_j$$

(44)

Stokes solved Eq. (44) with appropriate boundary conditions [$\mathbf{u} \to \mathbf{u}_0$ far away from the obstacles and no slip ($\mathbf{u} = 0$) on its surface] for flow past a circular cylinder of infinite length and past a sphere. The solution for a sphere is symmetric along the axis through the center of the sphere and in the direction of the unperturbed velocity far upstream:

$$u_r = u_0 \left(1 - \frac{3a}{2r} + \frac{a^3}{2r^3} \right) \cos \theta$$

$$u_\theta = -u_0 \left(1 - \frac{3a}{4r} - \frac{a^3}{4r^3} \right) \sin \theta$$

(45)

$$u_\phi = 0$$

where r, θ, and ϕ are spherical coordinates and a is the radius. Note that Stokes' solution also shows upstream–downstream symmetry, $\mathbf{u}(x, y, -z) = \mathbf{u}(x, y, z)$.

The drag force $\mathbf{F}_D$ can be calculated by integrating the stress tensor $S_{ij}(r, \theta)$ over the surface of the sphere and inserting (45),

$$F_{Di} = \int_{t=a} dS \, n_j S_{ij}(r, \theta)$$

with $\mathbf{n}$ being the surface normal; the stress tensor

$$S_{ij} = p\delta_{ij} - v\rho(\partial_j u_i + \partial_i u_j)$$

is given here in Cartesian form.

We define the drag coefficient C_D and the Reynolds number R as

$$C_D := \frac{\pi F_D}{\rho u_0^2 A} = \frac{\pi a F_D}{\rho v u_0 A R} \tag{46}$$

and

$$R := \frac{u_0 a}{v} \tag{47}$$

where a is the radius of the sphere or cylinder, F_D is the total drag force (cylinder: total drag force per unit length), and A is the cross section perpendicular to the unperturbed velocity (other authors use slightly different definitions; some use the diameter in the Reynolds number or do not include the factor π in the definition of the drag coefficient). Stokes' expression for the drag of a sphere then reads

$$C_D = \frac{6\pi}{R} \tag{48}$$

which is the famous Stokes formula of the textbooks.

Unfortunately, Stokes' solution is not a consistent approximation of the solution of the Navier–Stokes equations at low Reynolds numbers. This will be shown by calculating the advection and friction term using (45). First we rewrite the advection term as a sum of a gradient and a rotational part:

$$u_k \partial_k u_j = \tfrac{1}{2} \partial_j u^2 + \varepsilon_{jkl} \omega_k u_l \tag{49}$$

where $\omega_k = \varepsilon_{klm} \partial_l u_m$ is the vorticity. Stokes' solution is still valid if one adds the gradient $\tfrac{1}{2} \partial_j u^2$ to the pressure gradient [see Eq. (44)] because it is the general solution for a conservative distribution of viscous forces. The problematic term is the part describing the interaction of the induced vorticity with the flow. Using Stokes' solution (45), one gets at large distances r from the obstacle an order of magnitude of $u_0^2 a/r^2$ for the rotational term and $v u_0 a/r^3$ for the viscous term. Stokes' approximation breaks down when the ratio of the two terms is of the order of 1,

$$R \frac{r}{a} = O(1)$$

i.e., at a critical radius $r_c = a/R$.

4.2. Oseen's Approximation

In 1910 Oseen[31] proposed a new approximation now known as the Oseen equation:

$$u_{k0} \partial_k u_j = -\frac{1}{\rho} \partial_j p + \nu\, \partial_k \partial_k u_j \tag{50}$$

The equation is linear in **u** and formally it looks like the linearized Navier–Stokes equation, which can be derived with the ansatz $\mathbf{u} = \mathbf{u}_0 + \mathbf{u}_1$, where $\mathbf{u}_1$ is a small quantity. But near the obstacle the perturbation of the upstrem velocity is not small, because of the no-slip boundary condition. The idea of Oseen was to take into account the advection of momentum.[33] The left-hand side of (50) is small near the obstacle and does not contribute much to the boundary values. At larger distances it gives the linearized form of the advection. For the sphere an exact solution of the Oseen equation is not known. Although the Oseen approximation is justified only for low Reynolds numbers $(R \ll 1)$, approximate solutions will be shown for a far larger range of Reynolds numbers.

4.3. Oseen Flow Past a Sphere

In the literature there are several expressions available for the drag coefficient of a sphere. The following formulas are all based on the Oseen equation. Oseen[32] derived

$$C_D = \frac{6\pi}{R}\left(1 + \frac{3}{8} R\right) \tag{51}$$

based on an approximate solution. For a higher order of approximation Goldstein[14] got an analytic expression (corrected after Shanks; see ref. 27)

$$C_D = \frac{6\pi}{R}\left(1 + \frac{3}{8} R - \frac{19}{320} R^2 + \frac{71}{2560} R^3 - \frac{30179}{2150400} R^4 + \frac{122519}{17203200} R^5\right) \tag{52}$$

which is valid for $R \leqslant 2$ (for larger Reynolds numbers one needs numerical methods). The best analytically derived formula has been given by Mazur and Weisenborn.[27] The boundary condition at the surface of the sphere has been taken into account by an additional force (method of induced forces). They got

$$C_D = 8\pi \left[\xi(R) + \psi(R) - \frac{1}{2} \right.$$
$$\left. - \frac{[\xi(R) + 2\psi(R) - 1 - \frac{3}{2}R]^2}{[\xi(R) + \frac{9}{4}\psi(R) - \frac{7}{4} - \frac{1}{4}R^2 - \frac{1}{2}\exp(-2R)]} \right]^{-1} \tag{53}$$

with

$$\xi(R) = \gamma + \ln 2R - \text{Ei}(-2R)$$

$$\psi(R) = \frac{1}{4R^2} \left[1 - (1 + 2R)\exp(-2R) \right]$$

and $\gamma = 0.5772...$ is Euler's constant; $\text{Ei}(x)$ is the exponential integral

$$\text{Ei}(-x) = \gamma + \ln x - \int_0^x \frac{1 - e^{-y}}{y} \, dy, \qquad x > 0$$

In Fig. 10 (see Section 4.5) we plot the above functions together with the empirical formula of Zahm,[44]

$$C_D = 14\pi R^{-0.85} + 0.24 \qquad \text{for} \quad 0.2 < R < 200000 \tag{54}$$

and our numerical results.

4.4. Oseen Flow Past a Cylinder

As mentioned before, Stokes' approximation breaks down in the far field of the flow past a circular cylinder of infinite length. Stokes found a solution of the differential equation which satisfies the no-slip boundary condition but diverges for large distances. An analytical solution of the Oseen equation has been given by Faxén,[11] but it is not available in a form which enables one to obtain values for the drag coefficient.[40] In 1911 Lamb[24] gave the following expression based on an approximate solution of the Oseen equation:

$$C_D = \frac{4\pi}{R} \left[\frac{1}{2} - \gamma - \ln\left(\frac{R}{4}\right) \right]^{-1} \tag{55}$$

Other expressions can be found in ref. 40.

4.5. Drag Coefficients by Lattice Gas Simulations

Measuring drag coefficients with lattice gases serves as a proof for correct hydrodynamic behavior especially in the transitional range of

Reynolds numbers from laminar to slightly turbulent flow. It also provides an occasion to obtain quantitative results from lattice gas simulations. Two-dimensional flow simulations past a cylinder with the FHP lattice gas have been performed by Hayot and Lakshmi,[16] Duarte and Brosa,[10] and recently by Kohring,[22] who computed drag coefficients in two dimensions over four orders of magnitude in the Reynolds number $(0.1 < R < 300)$. All authors obtained very good agreement with numerical and experimental data.

In order to get an impression of the consequences of the anisotropic viscosity on the hydrodynamics of the PI lattice gas, we measured the drag coefficients of cylinders and spheres. We expect that the comparison with other data enables us to confirm the previously defined effective shear viscosity. For comparison we performed the two-dimensional simulations also with the FHP lattice gas.

Compared to other numerical techniques, the computation of drag coefficients with a lattice gas is an easy task even for a body of arbitrary shape. Recalling that the lattice gas approach is based on the simplified molecular dynamics of an ideal gas, it is reasonable that the force acting on the body can be directly computed via the number of particles scattered at its surface. To compute the momentum exchange ΔP, we simply have to count all particles hitting the body at every time step and sum up their changes of momentum parallel to the mean flow direction $\Delta v_i^{\parallel}$. We express the total drag force F_D from (46) as

$$F_D = \frac{\Delta P}{\Delta t} = \sum_{i=1}^{N} \Delta v_i^{\parallel}$$ (56)

with

$$N = \begin{cases} 2^D & \text{for} \quad \text{PI} \\ 6 & \text{for} \quad \text{FHP} \end{cases}$$

Note that $\Delta v_i^{\parallel}$ is the change of momentum per unit volume of the lattice, which has to be rescaled by 8/9 for the PI model $\frac{8}{9}\mathbf{q} = \mathbf{u}$. In the PI model one node contains 2^D unit volumes (cells). We have normalized mass and time step and use the distance between two lattice points as length unit (lu). For the FHP model one should remember that the hexagonal lattice scales with a factor of $\sqrt{\frac{3}{2}}$ in one direction. Due to the alternating grid (compare Fig. 1) the distance between two nodes of the PI lattice is $2\,lu$. For the two-dimensional case we have to replace the area A by the diameter L of the cylinder in (46).

The experimental setup consists of a channel twice as long as its width. Boundary conditions are periodic in the flow direction and free slip

(specular reflection of the particles) at the side walls. At the surface of the body a no-slip condition is imposed by reversion (bounce back) of hidding particles. When mapping the obstacle for the PI model one has to take into account that the PI model alternates between two slightly displaced sublattices. Therefore an obstacle defined on the whole lattice may have a different projection on each sublattice. A usage of the same representation for both sublattices would cause a worse representation of the obstacle shape. We tested both possibilities and found no significant effects on the drag.

Starting the simulation with a homogeneous velocity distribution, we compensated the damping due to the obstacle by inserting velocity profiles of the initial form at the upstream boundary. These profiles were selected at random from an initially prepared store in order to avoid additional perturbations. This initial situation corresponds to a sudden insertion of a solid body in a homogeneous flow, but after an adequate relaxation time the perturbations caused by this shock have disappeared and the flow becomes steady. Then we sample the drag coefficient according to (46) as a function of time.

The FHP experiments were made with constant density of $\rho = 1/6$ particles per cell and constant velocity of $u_0 = 0.21$. Different Reynolds numbers were obtained by scaling the whole domain and the obstacle.

The two-dimensional PI simulations were performed with constant grid sizes of (1024×512) nodes with an obstacle of 100 nodes in diameter.

For the three-dimensional simulations the domain size varied from $(64 \times 32 \times 32)$ nodes with a sphere of 6 nodes in diameter for the lowest Reynolds numbers to $(384 \times 192 \times 192)$ nodes with a 40-node sphere for the highest Reynolds numbers. The variation of the Reynolds number was done by initialization of different velocities for all PI simulations. The maximum possible velocity was $u_{max} = 0.21$, corresponding to a critical Mach number of $M_{crit} = 0.36$. Higher velocities degenerate to u_{max} during the simulation. For $M > 0.3$ the drag coefficient is not solely a function of the Reynolds number; instead it depends also on the Mach number.[36] The aspect ratio (e.g., the ratio of the channel width to obstacle length) was always 0.2 for all experiments.

Drag coefficients averaged over 10,000 time steps versus Reynolds numbers are displayed in Figs. 8–10.

Drag coefficients for spheres and cylinders have been derived from wind tunnel experiments by various authors (see, for example, refs. 39 and 36). In Figs. 8 and 9 we have additionally plotted the experimental results of Tritton[39] for reference. Figure 10 contains various analytical expressions for the drag coefficients together with the results of our numerical investigation. A fit of the data to Zahm's curve can be achieved with a shear viscosity of $\nu^{3D} = 0.21$, which we propose as effective shear viscosity.
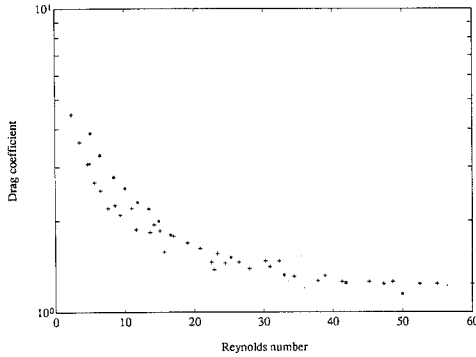
Fig. 8. Drag coefficient C_D of a cylinder versus Reynolds number R for the FHP (∗) lattice gas and experimental results from Tritton[39] (+). The shear viscosity is $v = 0.55$.

It is interesting to note that Stokes' formula for the sphere systemati-cally underestimates the drag, whereas the values based on the Oseen equa-tion overestimate the drag. Obviously the increase of drag by interaction of the induced vorticity with the flow is overestimated in Oseen's approx-imation. The asymptotic value of the drag coefficient at large Reynolds numbers is dominated by this interaction. The calculation of the drag coefficients at large Reynolds numbers is therefore a good test of the nonlinear advection of the lattice gas.

The Reynolds numbers are limited at low values by the ratio of signal to noise and by the mean free path, and at high values by the core memory of available computers (out-of-core computations are too ineffective) and the critical Mach number. We performed our simulations on a Convex C 2 with 64 MB and on a Cray Y-MP with 256 MB memory using the
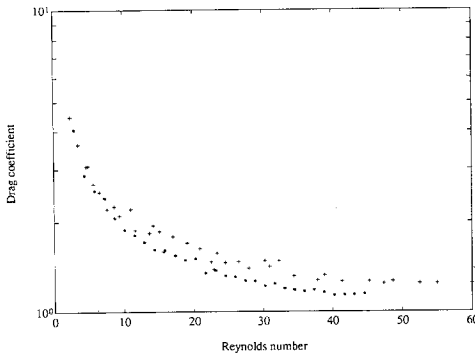

Fig. 9. Drag coefficient C_D of a cylinder versus Reynolds number R for the PI (∗) lattice gas and experimental results from Tritton[39] (+). The Reynolds numbers have been computed with an effective shear viscosity of $v_{\text{eff}}^{2D} = 0.35$.
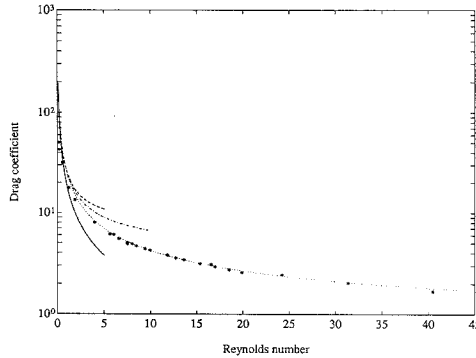
Fig. 10. Measured drag coefficient C_D for a sphere versus Reynolds number R for the PI lattice gas. The Reynolds numbers have been computed with an effective shear viscosity of $\nu_{\text{eff}}^{3D} = 0.21$ ($*$). It can be seen that our results match the empirical formula of Zahm ($\cdots$) very well. Analytical results by the Stokes theory (—), Oseen theory (--), and Oseen theory by Mazur and Weisenborn (-·-) are shown for comparison.

multispin coding technique in C. Typical values for the updating rates of the PI programs are 117 MUPS (million node updatings per second) for two dimensions and 29 MUPS for three dimensions on the Cray Y-MP (one processor). The Convex is approximately 32 times slower. A more detailed investigation of the performance of the PI model is found in ref. 41.

4.6. Finite-Size Effects

Besides other simplifications, lattice gas simulations deal with a relatively low number of particles compared to real gases. This limitation is caused by the restricted computational resources. In air, for example, under normal conditions we expect approximately $N_L = 2.69 \times 10^{25}$ particles/m^3 (N_L: Loschmidt number). A common lattice gas simulation contains not more than a few million particles. Especially when solid objects are involved, one has to check if the characteristic length l of the obstacle is still a macroscopic length. This means that it has to be large compared to the mean free path λ a particle travels between two collisions, or that the Knudsen number $\text{Kn} = \lambda/l$ has to be small. Otherwise so-called "finite-size effects" may become important and the Navier–Stokes equations not longer hold.

When simulating fluid flow through porous media, Rothman[34] was concerned with this problem of a relatively long mean free path of the FHP model running at low densities (approximately 10–12 lu at a density of one particle per node). Also, Kohring[20] found rather strong finite-size effects with the FHP-I model. He computed minimal mean free paths of 8 lu for

FHP-I and of 2–3 *lu* for FHP-II and for his own, new proposed model. Recent mean free path measurements by Chen *et al.*[3] yield a minimal value of 1.5 *lu* for the three-dimensional FCHC model.

We measured the mean free path of the PI model in two and three dimensions in order to assure that the minimal length scale of our simulations (diameter of the obstacle) is large compared to the mean free path, or that the Knudsen number remains small. Because of the stepwise pair interaction algorithm, it is not so easy to detect the number of collisions at a given node. By definition we speak of a collision when any of the $D + 1$ bits of a cell had been changed during the D interaction steps. Then we defined the mean free path λ as

$$\lambda := \frac{N_p \, |\mathbf{c}|}{N_{\text{col}}} \tag{57}$$

where N_p is the total number of particles, N_{col} is the number of collisions, and the factor $|\mathbf{c}| = \sqrt{D}$ is the propagation velocity of each particle. After relaxing 180 timesteps on a domain of 512×512 nodes, the two-dimensional result averaged over 20 timesteps on the whole domain is

$$\lambda_{2D} = 1.21 \, lu \tag{58}$$

For a cylinder of diameter 100 nodes this corresponds to a maximum Knudsen number of $\text{Kn} = 0.012$.

The same experiment on a three-dimensional domain of $128 \times 128 \times 128$ nodes yields

$$\lambda_{3D} = 1.22 \, lu \tag{59}$$

leading to a maximum Knudsen number of $\text{Kn} = 0.1$ for a sphere of diameter 6 nodes.

Furthermore, the implementation of the no-slip boundary condition by reversion of the particles has been investigated for artifical consequences by various authors. Cercignani[2] solved a linearized Boltzmann equation for the Kramer problem and plane Poiseuille flow. He found a shift of the parabolic velocity profile of second order in the Knudsen number. Concerning the velocity profile at a solid boundary, Lavallée *et al.*[25] found agreement between classical boundary layer theory[36] and calculations using the lattice Boltzmann equation as well as FHP lattice gas simulations. Ordinary boundary layer theory predicts the existence of a Knudsen layer of thickness $\approx \lambda$ at the boundary. Cornubert *et al.*[6] developed a Knudsen layer theory for the FHP model using the lattice Boltzmann

approximation. They concluded that the establishing of a Knudsen layer is prevented by the bounceback implementation, but the solid walls are effectively shifted by $1/4$ *lu* or $\sqrt{3}/4$ *lu*, depending on the orientation of the boundary relatively to the lattice (due to the geometric scaling factor of the FHP lattice). Although these results may basically also apply to the PI model, this kind of anisotropy is not to be expected here because of its different lattice structure. Even a displacement of approximately $1/2$ *lu* would increase the diameter of the obstacles, but the Reynolds number (47) and the drag coefficients (46) would not change significantly. Solely for the smallest diameter of 12 *lu* would this decrease the drag coefficient by about 15%, but this is partially compensated by an increase of the Reynolds number of 8%.

In order to check our PI simulations for further finite-size effects, which may be independent of the mean free path (or collision), we enlarged, respectively shrunk, the domain size (including obstacle) by a factor of two and found less than 10% deviation in the drag coefficient of the cylinder, which is comparable to the standard deviation. Deviations of less than 0.5% in the drag coefficient of the sphere are obtained for shrinking to $128 \times 64 \times 64$ nodes and expanding to $384 \times 192 \times 192$ nodes at a Reynolds number of 9.

5. SUMMARY AND CONCLUSIONS

Hydrodynamic equations for the compressible viscid regime have been derived and the dissipation of the pair interaction automaton has been investigated with the wave relaxation method. The shear viscosity is strongly anisotropic: the maximum of the shear viscosity is twice as large as the minimum. The radial dependence of the relaxation constant shows good agreement (same phase; differences in the amplitude of less than 10%) with theoretical predictions based on the Boltzmann equation. The compressional viscosity is also strongly anisotropic.

Effective viscosities of $v_{eff} = 0.35$ in two dimensions and $v_{eff} = 0.21$ in three dimensions have been postulated for practical use. Simulations of hydrodynamic flows in two and (for the first time with PI) three dimensions were performed. The flow fields show qualitative agreement with wind tunnel experiments (formation and shedding of eddies at large Reynolds numbers). Despite the unusual behavior of the viscosity, the drag coefficients for flow past cylinders of infinite length and spheres show very good quantitative agreement with experimental values when the Reynolds numbers are computed with the effective viscosities. A fit of the drag data yields a viscosity of $v^{3D} = 0.24$. The range of investigated Reynolds numbers is 5–50 in two and 0.9–40 in three dimensions.

The low sensitivity to finite-size effects demonstrates the good suitability of the PI for low-Reynolds-number flow simulations in complex geometries (e.g., porous media). However, a detailed investigation of the PI model with respect to the results of ref. 6 seems to be useful, but is left for future work.

Another question that remains to be investigated is the anisotropy of the collision process with respect to axis exchange. The fixed succession of interaction directions may cause an additional anisotropy, not detectable by the wave relaxation method. It could lead to a nonvanishing lift of an obstacle when the flow is not parallel to a coordinate axis. This effect may be removed by random permutations of the interaction succession.

The results—especially in three dimensions— are encouraging for the simulation of more complex flow problems with the PI. Although PI needs more bits per node than FCHC (32 compared to 24), we prefer the former because of its simple modular structured interaction rules, allowing vectorizable multispin coding (see refs. 21 and 41) with Boolean functions even in the three-dimensional case. A straightforward construction of a lookup table for FCHC with its $2^{24} = 16,777,216$ possible states per node requires a memory of up to 100 Mbyte. Some encouraging strategies to reduce this memory requirement have been proposed by Hénon[17] and Somers and Rem[37] (to 64 kbyte), but the applications of this model are still very rare. This may be due to its more complicated structure.

ACKNOWLEDGMENTS

REFERENCES

1. D. Burgess, F. Hayot, and W. F. Saam, Model for surface tension in lattice-gas hydrodynamics, *Phys. Rev. A* **38**(7):3589–3592 (1988).
2. C. Cercignani, Kinetic theory with "bounce-back" boundary conditions, *Transport Theory Stat. Phys.* **18**(1):125–131 (1989).
3. S. Chen, K. Diemer, G. D. Doolen, K. Eggert, C. Fu, S. Gutman, and B. J. Travis, Lattice gas automata for flow through porous media, *Physica D* **47**:72–84 (1991).
4. S. Chen, M. Lee, K. H. Zhao, and G. D. Doolen, A lattice gas model with temperature, *Physica D* **37**:42–59 (1989).
5. P. Clavin, P. Lallemand, Y. Pomeau, and G. Searby, Simulation of free boundaries in flow systems by lattice-gas models, *J. Fluid Mech.* **188**:437–464 (1988).
6. R. Cornubert, D. d'Humières, and D. Levermore, A Knudsen layer theory for lattice gases, *Physica D* **47**:241–259 (1991).

7. D. d'Humières and P. Lallemand, Lattice gas automata for fluid mechanics, *Physica A* **140**:326–335 (1986).
8. D. d'Humières and P. Lallemand, Numerical simulations of hydrodynamics with lattice gas automata in two dimensions, *Complex Syst.* **1**(4):598–632 (1987).
9. D. d'Humières, P. Lallemand, and U. Frisch, Lattice gas models for 3D hydrodynamics, *Europhys. Lett.* **2**:291–297 (1986).
10. J. A. M. S. Duarte and U. Brosa, Viscous drag by cellular automata, *J. Stat. Phys.* **59**(1/2):501–508 (1989).
11. H. Faxén, *Nova Acta Reg. Soc. Scient. Ups.* (vol. ex ord. ed., 1927).
12. U. Frisch, D. d'Humières, B. Hasslacher, P. Lallemand, Y. Pomeau, and J.-P. Rivet, Lattice gas hydrodynamics in two and three dimensions, *Complex Syst.* **1**:649–707 (1987).
13. U. Frisch, B. Hasslacher, and Y. Pomeau, Lattice-gas automata for Navier–Stokes equations, *Phys. Rev. Lett.* **56**:1505–1508 (1986).
14. S. Goldstein, The steady flow of viscous fluid past a fixed spherical obstacle at small Reynolds numbers, *Proc. R. Soc. Lond. A* **123**:225–235 (1929).
15. J. Hardy, Y. Pomeau, and de Pazzis, O. Time evolution of a two-dimensional model system. I. Invariant states and time correlation functions, *J. Math. Phys.* **14**(12):1746–1759 (1973).
16. F. Hayot and M. R. Lakshmi, Cylinder wake in lattice gas hydrodynamics, *Physica D* **40**:415–420 (1989).
17. M. Hénon, Isometric collision rules for four-dimensional FCHC lattice gas, *Complex Syst.* **1**(3):475–494 (1987).
18. M. Hénon, Viscosity of a lattice gas, *Complex Syst.* **1**(4):762–790 (1987).
19. J. Huang, Y. Chu, and C. Yin, Lattice-gas automata for modeling acoustic wave propagation in inhomogeneous media, *Geol. Res. Lett.* **15**(11):1239–1241 (1988).
20. G. Kohring, Using cellular automata for modeling fluid flows in porous media, Invited talk presented at the Seminar I Petroleumsfysikk, Stavanger, Norway (August 15–16, 1992).
21. G. A. Kohring, Parallelization of short- and long-range cellular automata on scalar, vector, SIMD and MIMD machines, *J. Mod. Phys. C* **2**(3):755–772 (1991).
22. G. A. Kohring, Calculations of drag coefficients via hydrodynamic cellular automata, *J. Phys. II* (Paris) **2**:265–269 (1992).
23. C. F. Kougias, Simulating a small-scale oceanic front of river discharge type with the lattice gas automata method, Ph.D. thesis, Universität Oldenburg (1991).
24. H. Lamb, *Hydrodynamics* (Cambridge University Press, Cambridge, 1932).
25. P. Lavallée, J. P. Boon, and A. Noullez, Boundary interactions in a lattice gas, in *Proceedings of the Workshop on Discrete Kinetic Theory, Lattice Gas Dynamics and Foundations of Hydrodynamics, Torino, Italy, 1988*, R. Monaco, ed. (World Scientific, Singapore, 1989), pp. 160–162.
26. H. Lim, Cellular-automaton simulations of simple boundary-layer problems, *Phys. Rev. A* **40**(2):968–980 (1989).
27. P. Mazur and A. J. Weisenborn, The Oseen drag on a sphere and the method of induced forces, *Physica A* **123**:209–226 (1984).
28. K. Molvig, P. Donis, R. Miller, J. Myczkowski, and G. Vichniac, Multispecies lattice-gas automata for realistic fluid dynamics, in *Cellular Automata and Modeling of Complex Physical Systems*, G. Y. Vichiniac, P. Manneville, N. Boccara, and R. Bidaux, eds. (Springer-Verlag, 1989), pp. 206–232.
29. D. Montgomery and G. D. Doolen, Two cellular automata for plasma computations, *Complex Syst.* **1**:830–838 (1987).

30. R. Nasilowski, A cellular-automaton fluid model with simple rules in arbitrary many dimensions, *J. Stat. Phys.* **65**:97–138 (1991).
31. C. W. Oseen, Über die Stokes'sche Formel, und über eine verwandte Aufgabe in der Hydrodynamik, *Ark. Mat. Astr. Fys.* **6**(29):1–20 (1910).
32. C. W. Oseen, Über den Gültigkeitsbereich der Stokesschen Widerstandsformel, *Ark. Mat. Astr. Fys.* **9**(16):1–15 (1913).
33. I. Proudman and J. R. A. Pearson, Expansions at small Reynolds numbers for the flow past a sphere and a circular cylinder, *J. Fluid Mech.* **2**:237–262 (1957).
34. D. H. Rothman, Cellular-automaton fluids: A model for flow in porous media, *Geophysics* **53**(4):509–518 (1988).
35. D. H. Rothman and J. M. Keller, Immiscible cellular-automaton fluids, *J. Stat. Phys.* **52**:1119–1127 (1988).
36. H. Schlichting, *Grenzschicht-Theorie* (Verlag G. Braun, Karlsruhe, 1982).
37. J. A. Somers and P. C. Rem, The construction of efficient collision tables for fluid flow computations with cellular automata, in *Cellular Automata and Modeling of Complex Physical Systems*, G. Y. Vichiniac, P. Manneville, N. Boccara, and R. Bidaux, eds. (Springer-Verlag, 1989), pp. 206–232.
38. G. G. Stokes, On the effect of internal friction of fluids on the motion of pendulums, *Trans. Camb. Phil. Soc.* **9**:8–106 (1851).
39. D. J. Tritton, Experiments on the flow past a circular cylinder at low Reynolds numbers, *J. Fluid Mech.* **6**:547–567 (1959).
40. A. J. Weisenborn and P. Mazur, The Oseen drag on a cylinder revisited, *Physica* **123A**:191–208 (1984).
41. D. A. Wolf-Gladrow and A. Vogeler, Pair interaction lattice gas on general purpose computers: FORTRAN or C? *Int. J. Mod. Phys. C*, to be published.
42. D. A. Wolf-Gladrow, R. Nasilowski, and A. Vogeler, Numerical simulations of fluid dynamics with a pair interaction automaton in two dimensions, *Complex Syst.* **5**:89–100 (1991).
43. S. Wolfram, Cellular automaton fluids 1: Basic theory, *J. Stat. Phys.* **45**:471–526 (1986).
44. Zahm, Technical Report 253, National Advisory Committee for Aeronautics (1923).